Images of the East African Rift System by Global Adaptive-Resolution Surface-Wave Tomography

Félicie Korostelev, Yang Lu, Fabrizio Magrini, Lapo Boschi, Sylvie Leroy, William Vétel

Images of the East African Rift System by Global Adaptive-Resolution Surface-Wave Tomography

Félicie Korostelev[1], Yang Lu[2,3], Fabrizio Magrini[4,5], Lapo Boschi[1,6], Sylvie Leroy[1], William Vétel[7]

[1]Sorbonne Université, CNRS, INSU, Institut des Sciences de la Terre de Paris, ISTeP UMR 7193, F-75005 Paris, France.

[2]Department of Earth Sciences, University of Southern California, USA

[3]Department of Meteorology and Geophysics, University of Vienna, Austria

[4]Department of Geological Science, Università degli Studi Roma Tre, Italy

[5]Institute of Geosciences, Johannes Gutenberg University, Mainz, Germany

[6]Dipartimento di Geoscienze, Università degli Studi di Padova, Italy

[7]Total Exploration et Production, Pau, France

Key Points:

- Joint inversion of global and regional phase-velocity measurements using an adaptive parameterization
- Global phase-velocity maps characterized by an improved resolution throughout the East African Rift System
- Low-velocity anomaly beneath Mozambique Channel probably ascribed to a significant magmatic system

Corresponding author: Félicie Korostelev, `felicie.korostelev@gmail.com`

Abstract

In this study we map the entire East African Rift System (EARS) within a global surface-wave velocity model to better constrain the structure of the underlying mantle, as well as patterns that might be associated with its continuation in the Mozambique Channel. We use all publicly available seismograms from the African continent, amounting to 1296 stations and more than 30 years of recordings. From these data, we obtain dispersion curves using both ambient noise and teleseismic earthquakes. To our measurements, we add global counterparts and jointly invert them for phase-velocity maps. We exploit a linearized inversion based on the ray theory, with an adaptive parameterization that allows for maximizing the resolution of the final maps based on the density of data coverage. We thus image the main African cratons and also some of the Archean blocks within them. We highlight the discontinuous nature of magmatic activity along the EARS and also display low-velocity anomalies beneath the Comores Archipelago, Madagascar and Bassas da India volcanic islands and seamounts. This last low-velocity anomaly is in the direct continuation of the EARS and could unveil an important magmatic system in the Mozambique Channel.

Plain Language Summary

The East African Rift System (EARS) is where tectonic plates are breaking and drifting apart in Africa. The opening of the EARS most probably finds its origin in the forces existing in the underlying mantle. The goal of this study is to better understand the structure of the inside of the Earth in the region. To do that, we use waves registered by seismometers to create maps of the crust and upper mantle (the lithosphere). These maps display where the waves travel at different speed, giving us information about the Earth's structure. In our maps of wave speed, we see several very interesting things. First, we see fast speeds in areas of thick lithosphere (cratons), and our resolution gives us some details on their inner structure. Then, we see three patches of slow speeds along the EARS, suggesting that this system is discontinuous, with some very active points where volcanic fields are present. Finally, we see slow speeds in the Mozambique Channel, where no such feature was reported before. This suggests that the lithosphere is hot there and perhaps contains some melt. This may show the development of the EARS southwards into the Mozambique Channel.

1 Introduction

The East African Rift system (EARS) is a complex feature that runs approximately from north to south in East Africa, i.e. from Eritrea, Djibouti and Ethiopia to Mozambique (McConnell, 1972; Chorowicz, 2005; Ring, 2014). At its northern end, the EARS connects to the Red Sea and Gulf of Aden rifts in the wide Afar depression. The Main Ethiopian Rift is located directly south of the Afar depression. Afar and the Main Ethiopian Rift are characterized by active magmatic segments in which extension mainly occurs (Ebinger & Casey, 2001). Further south, the EARS splits into two branches that surround the Tanzanian craton (see fig. 1). The eastern branch (B. H. Baker et al., 1972; Ebinger, 2005) consists of the wide Turkana Depression and the Kenya narrow rift. The western branch (Ebinger, 1989; Daly et al., 1989) is composed of the Albert-Edward (NE-SW), Kivu (N-S) and Tanganyika-Rukwa (NW-SE) rifts (fig.1). It is prolongated in the south by the Malawi rift (Ring et al., 1992; Laó-Dávila et al., 2015) that has an active volcanic province at its northern end: the Rungwe volcanic province, in Tanzania (Ebinger, 1989; Fontijn et al., 2012; Borrego et al., 2018).

The emergence of the EARS is linked to an extensive volcanic activity with voluminous Tertiary flood basalts on the Ethiopian high plateaus, and is possibly due to one, two or three mantle plumes (e.g., Bastow et al., 2008; Benoit et al., 2006; Hansen & Nyblade, 2013; Ritsema et al., 2011; S.-J. Chang et al., 2020). Its particular geometry is ascribed to the location of different Archean cratons (McConnell, 1972; Mohr, 1982). The eastern and western branches circle the Archean Tanzanian craton (Bell & Dodson, 1981; Chesley et al., 1999; Manya, 2011). The Western branch is flanked in the west by the Congo craton (De Waele et al., 2008), composed of several smaller blocks. To the south, the Zimbabwe, Kaapval and Kalahari cratons are the main large-scale structures (Nguuri et al., 2001; Jacobs et al., 2008) (fig. 1).

The African continent, and more particularly its eastern part, has been widely studied in the last decades, but not thoroughly characterized. Several seismological studies (e.g., Korostelev et al., 2015; Adams et al., 2018; Plasman et al., 2019; White-Gaynor et al., 2020; Clutier et al., 2021) only focused on the small-scale structure of specific parts of the EARS, based on temporary and permanent seismic networks deployed in the respective regions of interest. On the contrary, global studies (e.g., Ekström, 2011; Auer et al., 2014; Ruan et al., 2019; Celli et al., 2020) can only afford a coarser resolution, and display the Afar and Main

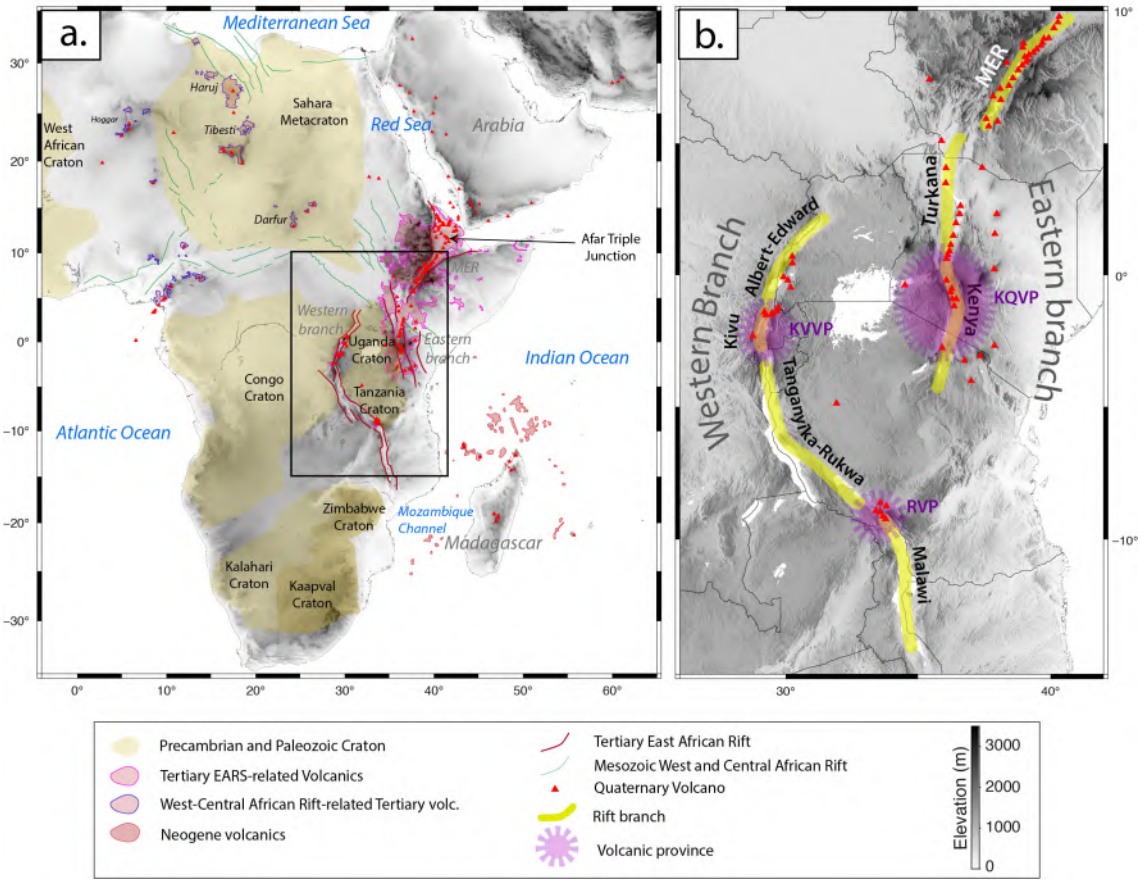

Figure 1. a. Structural map of our interest region, showing the location and extent of the Archean cratons, Tertiary volcanism and EARS main structures. Red triangles are volcanoes (modified from Global Volcanism Program (2013)). Structures are from Globig et al. (2016). b. Map of the EARS showing the main rifts and volcanic provinces. Abbreviations: KVVP Kivu Virunga Volcanic Province, KQVP Kenya Quaternary Volcanic Province, RVP Rungwe Volcanic Province, MER Main Ethiopian Rift.

Ethiopian Rift as a large low velocity anomaly in the upper mantle, and the South African Superswell in the lower mantle (Ritsema et al., 1999; Davaille & Romanowicz, 2020).

The aim of this study is to enhance the resolution of the seismic images of the EARS. To do that, we use publicly available seismograms to obtain Rayleigh-wave dispersion curves. We combine these dispersion curves with the global ones measured by Ekström (2011). We then translate the collected dispersion curves into global maps using a linearized inversion based on the ray theory, as explained in section 3. Our inversion scheme allows for an adaptive parameterization based on the density of data coverage, that enables us to obtain a global model characterized by an improved resolution across Eastern Africa in comparison with previous studies. We present the results and our interpretation of the most relevant features of our maps in section 4. A 3D analysis will be the subject of a future study based on a larger regional dataset.

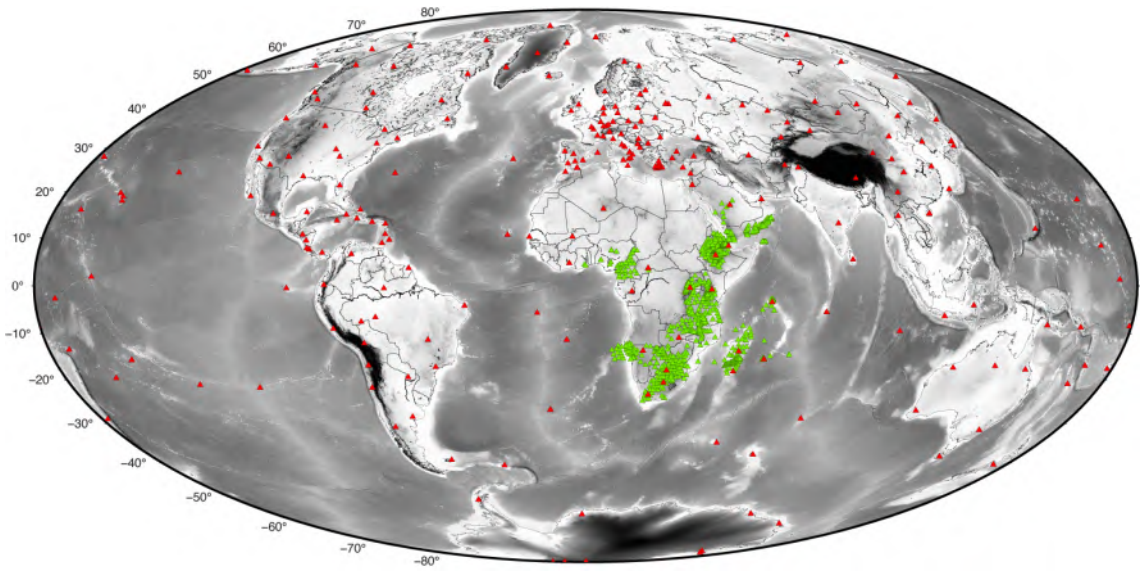

Figure 2. Regional and global datasets. Stations from global dataset are shown in red (Ekström, 2011), stations from regional dataset are shown in green. Regional stations are mainly located along eastern Africa, with a particularly dense coverage over the Afar rift (Ethiopia).

2 Rayleigh-wave phase-velocities

We download publicly-available seismograms from 54 seismic networks (fig. 2): 10 permanent and 44 temporary ones. The geographic distribution of the sensors, which is

particularly dense across the eastern part of Africa, provides us with a relatively good seismic coverage of the EARS.

We process the seismic data following two different criteria, detailed below, to obtain measurements of fundamental-mode Rayleigh-wave phase-velocities between pairs of sensors. The phase-velocities are calculated based on both teleseismic earthquakes (EQ) and seismic ambient noise (AN). The two datasets carry complementary information (e.g., Zhou et al., 2012): while ambient noise is dominated by relatively high frequencies and thus provides information on shallow structures, teleseismic data are sensitive to deeper parts of the Earth.

2.1 Seismic ambient noise

We exploit continuous recordings obtained on the vertical component of 1,231 seismic sensors belonging to 54 regional networks located in Africa and deployed between 1980 and 2017. We use these seismograms to obtain 38,469 inter-station phase velocities of AN generated Rayleigh waves, using the automated algorithm of Kästle et al. (2016). In practice, for each pair of stations that recorded simultaneously for at least six months, we subdivide their continuous seismograms into overlapping (50%) one-hour-long time windows. In each temporal interval, we apply spectral whitening (Bensen et al., 2007) to mitigate the effects of anomalous signals such as strong local earthquakes or anthropic noise (Boschi et al., 2013). Then we cross correlate the waveforms of the two sensors daily in the frequency domain. The daily cross-correlations are added to one another, or 'stacked' to obtain a unique, robust cross-spectrum, and that can be used to extract the inter-station dispersion curve as explained in Ekström et al. (2009).

Our measurements cover the period range 3-200 s, with a maximum number of measurements below 50 s (fig. 3a). In this study, we only focus on measurements recorded between 10 and 100 s. Measurements below 25 s cannot be inverted jointly with the global dataset of Ekström (2011) because it does not offer data below 25 s. Usually, AN is used for periods up to 50 to 60 s (e.g., Magrini et al., 2020). However, some studies showed that greater periods are also reliable (e.g., Luo et al., 2015; Emry et al., 2019).

2.2 Teleseisms

We exploit 1,328 teleseismic events recorded by 1,207 public sensors from 54 global or regional networks located in Africa and deployed from 1980 to 2017. We select teleseismic

events distant of 20° to 150° from recording stations, with a minimum magnitude of 6.5 to get a good signal/noise ratio (fig. 4). This results in 38,390 triplets of stations and sources approximately lying along the same great circle path.

We calculate earthquake-based (EQ) phase velocities using a two-station method (e.g., Meier et al., 2004; Soomro et al., 2016), based on the automated algorithm of Magrini et al. (2020). The two-station method measures the frequency-dependent phase delay of a surface wave observed at pairs of sensors that are approximately aligned on the same great circle path as the epicenter (we set the maximum azimuthal deviation to 5°). Via tight bandpass filters, the delay is calculated at discrete periods by cross-correlation and used to retrieve the phase-velocity through the dispersion relation (Magrini et al., 2020). For each station pair, the final measurement is calculated as an average carried out over at least three dispersion curves (corresponding to an equal number of earthquakes). Station pairs associated with less than three earthquakes or with dispersion curves characterized by relatively large standard deviations (we follow the Interquartile Range rule (Tukey, 1977) with outlier constant set to 0.1) are discarded.

To account for possible deviations from the great-circle path in the wave propagation, we apply a procedure which Magrini et al. (2020) refer to as "arrival-angle correction". In practice, the dispersion measurements are corrected by measuring the arrival azimuth of the Rayleigh-waves at the sensors. The arrival angle is used to convert apparent phase velocity into true phase velocity (eq.(11) of Magrini et al., 2020). We obtain 10,362 dispersion curves without correction and 7,233 dispersion curves with the arrival-angle correction. As illustrated in figure 3b, the difference between EQ and AN is always small (less than 0.05 km/s), which means that EQ and AN data are compatible. The arrival-angle correction has the effect of reducing the bias until at least 60 seconds. This bias is commonly amounting to few percentage points (e.g., Yao et al., 2006; Kästle et al., 2016). Above 60 seconds the correction is not obviously useful, but the bias remains smaller than 0.02 km/s.

2.3 Global dataset

To enhance the data coverage in regions characterized by relatively few interstation paths, we additionally take advantage of a global-scale, relatively long period database of surface-wave dispersion. The global dataset was compiled by Ekström (2011) and consists of surface-wave phase-velocity anomalies with respect to PREM (Dziewonski & Anderson,

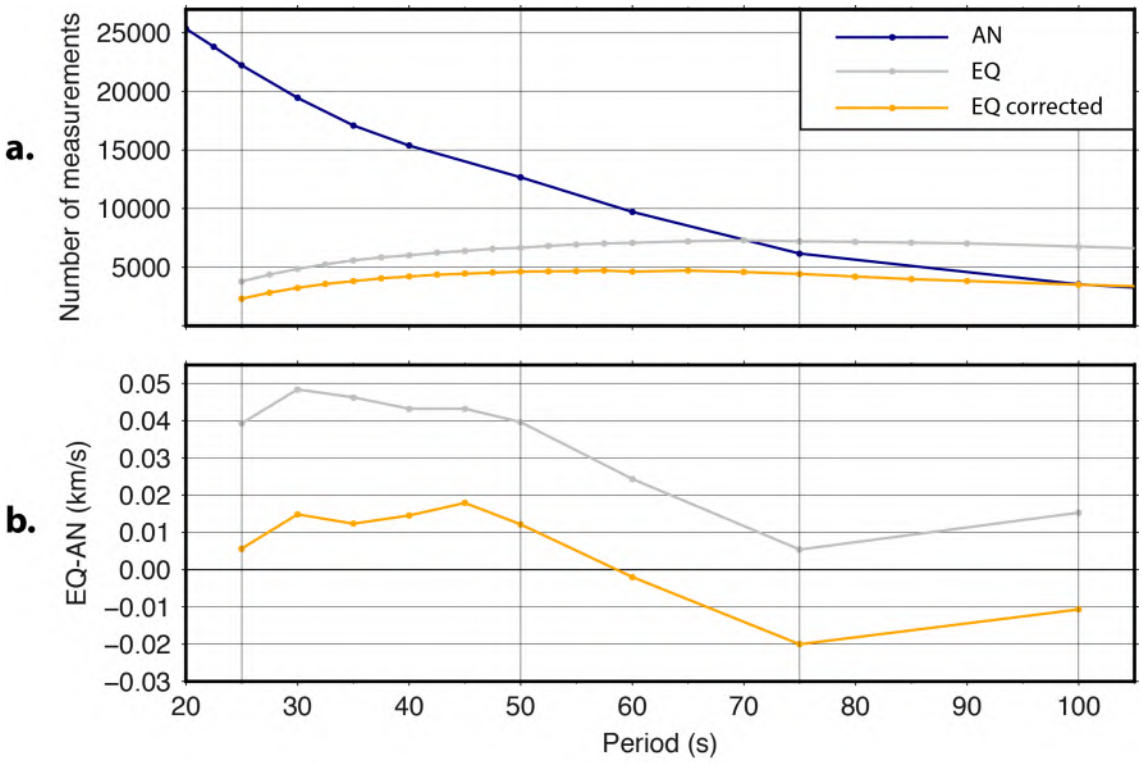

Figure 3. a. Number of measurements available for each method as function of period: ambient noise (AN) in blue, and earthquake (EQ) in orange and grey, with and without arrival-angle correction, respectively. b. Differences between the dispersion curves obtained from the ambient noise and teleseisms methods, averaged over all pairs.

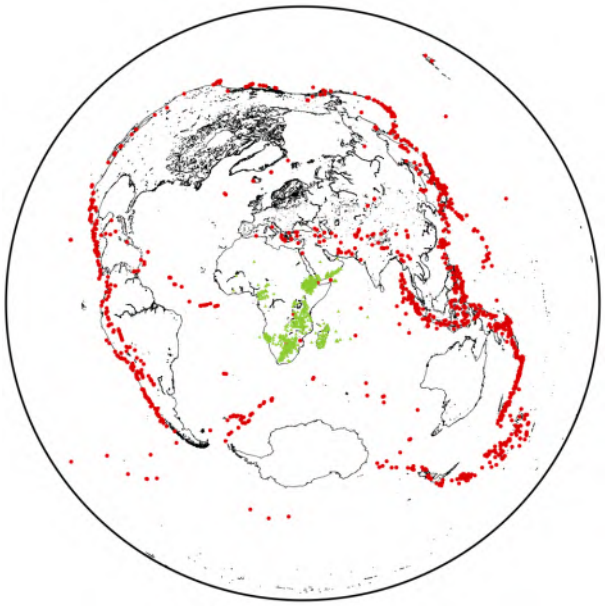

Figure 4. Teleseismic events exploited in this study are in red. Sensors from regional dataset are shown in green.

1981). We make use of Rayleigh-wave phase-velocity measurements of 3,330 teleseisms by 258 seismographic stations (fig. 2) located all over the globe (Ekström, 2011).

We also compare delays obtained from regional and global datasets in order to assess the coherence of both datasets. Delays are the difference in travel times between observed and predicted Rayleigh waves and are calculated relative to the Preliminary Reference Earth Model (known as PREM) of Dziewonski and Anderson (1981). Figure 5 shows the distribution of delays from global (red) and regional (blue) datasets. Global delays spread over a wider range than regional ones. Regional dataset also displays a light shift towards slower delays at short period (25 s). This could be explained by the fact that regional networks mainly lie on eastern Africa, where the EARS displays low velocity features (e.g. Bastow et al., 2005; S. Chang et al., 2011; Adams et al., 2018). However, regional delays fall within the range of global delays.

3 From dispersion curves to phase-velocity maps

At discrete periods, we use the dispersion curves calculated as explained in Section 2 to compute Rayleigh-wave travel times between pairs of sensors with the forward problem formulated under infinite-frequency ray approximation. The surface-waves are assumed to propagate only on the surface of the Earth and only along the great-circle path connecting sensor-sensor (for AN) or epicenter-sensor (for EQ). The inversion method used here is originally formulated in Boschi and Dziewonski (1999), and further elaborated in many recent studies (e.g., Schaefer et al., 2011; Lu et al., 2018). In the following, we describe our technical implementation, but more theoretical details could be found in the literature as listed above.

Adaptive parameterization has been the subject of many tomographic studies (e.g., Curtis & Snieder, 1997; Bodin & Sambridge, 2009; Schaefer et al., 2011). These methods aim at building an optimal model grid that matches the spatial variability of seismic data content to better condition the inverse problem. This is particularly important in studies attempting to integrate the results of local and global tomography, despite the significant discrepancy in data density within the region of interest and in the rest of the globe. Here, we use an adaptive parameterization algorithm following Schaefer et al. (2011). We define an adaptive grid depending on ray-path density using a four-level stepwise refining process. The model is first discretized on an initial equal-area uniform grid with coarse (3° x 3°) node

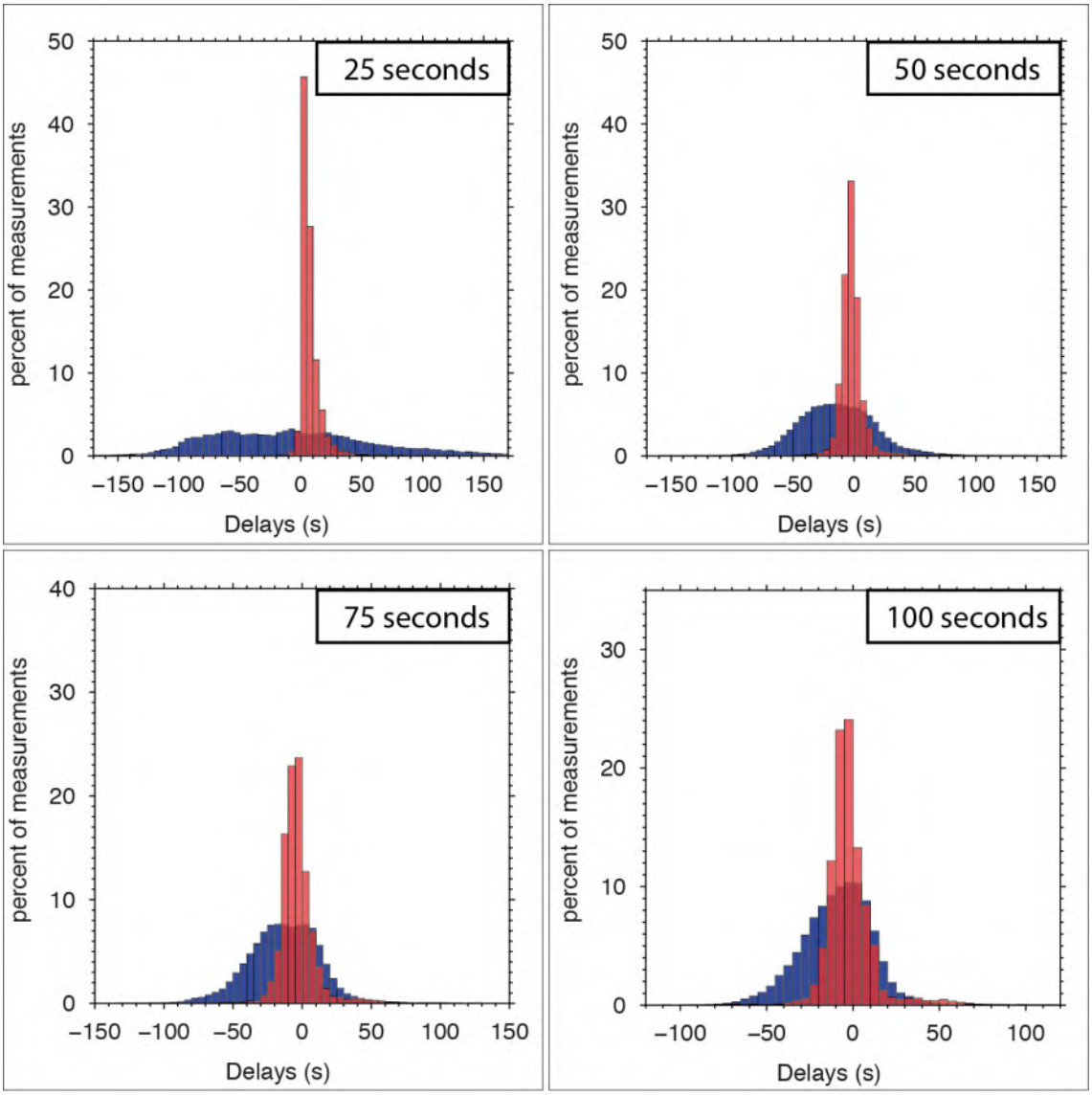

Figure 5. Distribution of Rayleigh-wave phase delays measured from global (blue) and regional (red) datasets at the periods of 25, 50, 75, and 100 s in percent. Delays are the difference in travel times between observed and predicted Rayleigh waves and are calculated relative to the Preliminary Reference Earth Model (known as PREM) of Dziewonski and Anderson (1981). Global data are from the study of Ekström (2011). Regional data are from 2-station observations of Rayleigh waves from both noise and teleseisms.

188 spacing, and then the grid cells intersected by more than 4000 great-circle paths associated
189 with surface-wave measurements are iteratively refined in three steps. In each step, any
190 grid cell meeting a preset number of intersecting great-circle paths (4000 hitcounts here)
191 will be further split into four smaller cells. The final constructed grid allows for eight
192 times of node spacing differences between the coarsest grid cell and the finest one (0.375°
x
193 0.375°).This procedure implicitly contributes to regularize the inverse problem by optimizing
194 the constraints given by the data on each model parameter. This also results in a better
195 resolution in the regions characterized by good data coverage.

196 The tomographic problem is usually solved in the least square sense with regularization
197 to reduce instabilities in the solution. Following Boschi and Dziewonski (1999), we define
198 the linear inverse problem in the following matrix form

$$\begin{bmatrix} \mathbf{A} \\ \mu\mathbf{G} \end{bmatrix} * x = \begin{bmatrix} \mathbf{d} \\ \mathbf{0} \end{bmatrix} \tag{1}$$

199

200

201

202 where the first relation $A * x = d$ describes the generally ill-conditioned forward prob-
203 lem, and the second relation represents the roughness damping regularization term. In the
204 first relation, the matrix A denotes the kernels discretized in the grid basis, d the data, and
205 x the model unknowns. μ denotes the weight assigned to the regularization constraint, and
206 G the first-order differential operator of model parameter x with respect to location.

207 Roughness damping imposes a regional smoothing effect by minimizing the gradient of
208 the model solution, thus removing the bias toward the initial model. The assumption of
209 regional smoothness is actually reasonable seeing that small-scale heterogeneities would not
210 be properly accounted for in a ray-approximation tomographic framework, and smoothing
211 somewhat ends up playing the role of finite frequency kernels (De Hoop & van Der Hilst,
212 2005). The roughness damping term is implemented by the differential operator G, which
213 implies the first-order smoothness for adjacent grid cells. The solution of the linear problem
214 is approximated via an iterative LSQR algorithm (Paige & Saunders, 1982).

4 Results and discussion

4.1 Checkerboard Test

Synthetic checkerboard tests are computed in order to investigate the robustness of the solution model for large- and small-scale velocity anomalies. For these tests we use the same pairs of stations as in our dataset to predict the Rayleigh-wave phase-velocities for a synthetic checkerboard structure.

The large-scale checkerboard consists of 15° x 15° anomalies that alternate between slow (-10%) and fast (+10%) velocity (see fig. 6). The dataset calculated through this synthetic velocity model is then inverted, and the retrieved velocity variations provide an indication of the resolution that can be achieved in our solution velocity model (shown in fig. 6). At all periods, the 15° x 15° checkerboard pattern is retrieved well by our global dataset. We notice that resolution is higher from 50 seconds on, which can be explained by the larger size of the global dataset at these periods. The resolution is poorer at the poles due to reduced station density and data coverage.

Figure 7 shows the small-scale checkerboard test, illustrating the resolution provided by regional networks in Africa. The exact same dataset as for the global test is used, but the checkerboard consists of 3° x 3° velocity anomalies separated by 1.5° gaps (input model in fig. 7). Solution models shown in figure 7 confirm the best resolution is obtained in the areas covered by most stations, where we can resolve structures of a lateral extent down to 3°. The 3° blocks are too small to be resolved beneath western Africa and under the oceans.

Figure 8 shows two checkerboard resolution tests at 10 s. The first one displays 6° x 6° checkers whereas the second one displays 3° x 3° checkers. At this period we are able to retrieve the anomalies along the EARS, southern Africa and Madagascar, which are the areas with the best data coverage.

4.2 Maps

Following the procedure explained in section 3, we obtained phase-velocity maps at different surface-wave periods at both global (fig. 9) scale and regional (fig. 10) scale. Our global phase-velocity maps display all the prominent features of those of Ekström (2011) at the same periods, such as cratonic areas and mid-oceanic ridges for instance. The

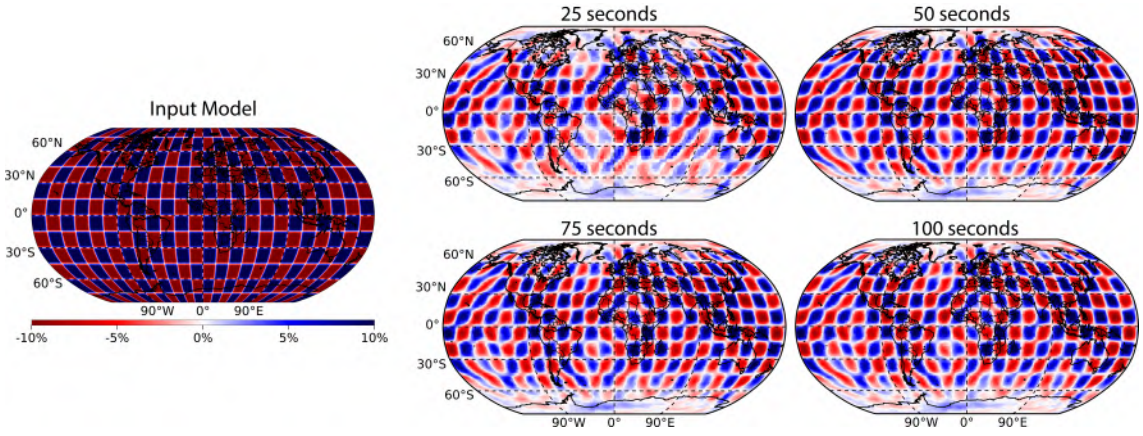

Figure 6. Large-scale checkerboard test. Left panel shows the input model, solution models for 25, 50, 75 and 100 s are to the right.

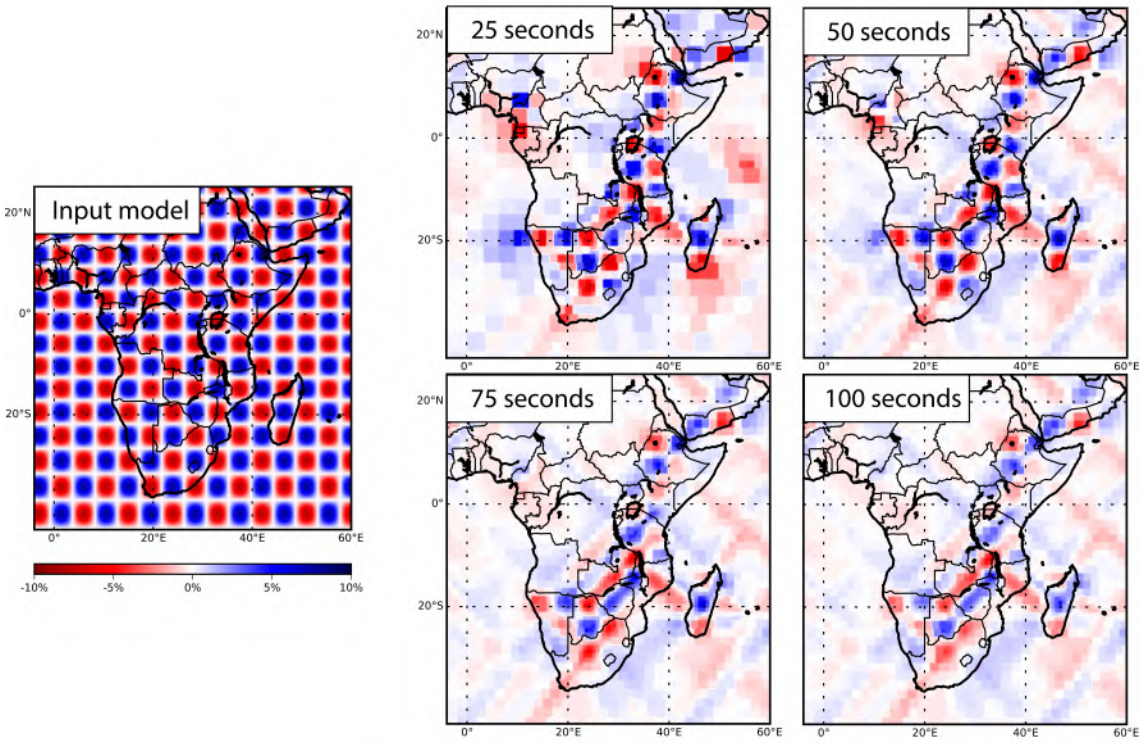

Figure 7. Small-scale checkerboard test. Left panel shows the input model, solution models for 25, 50, 75 and 100 s are to the right.

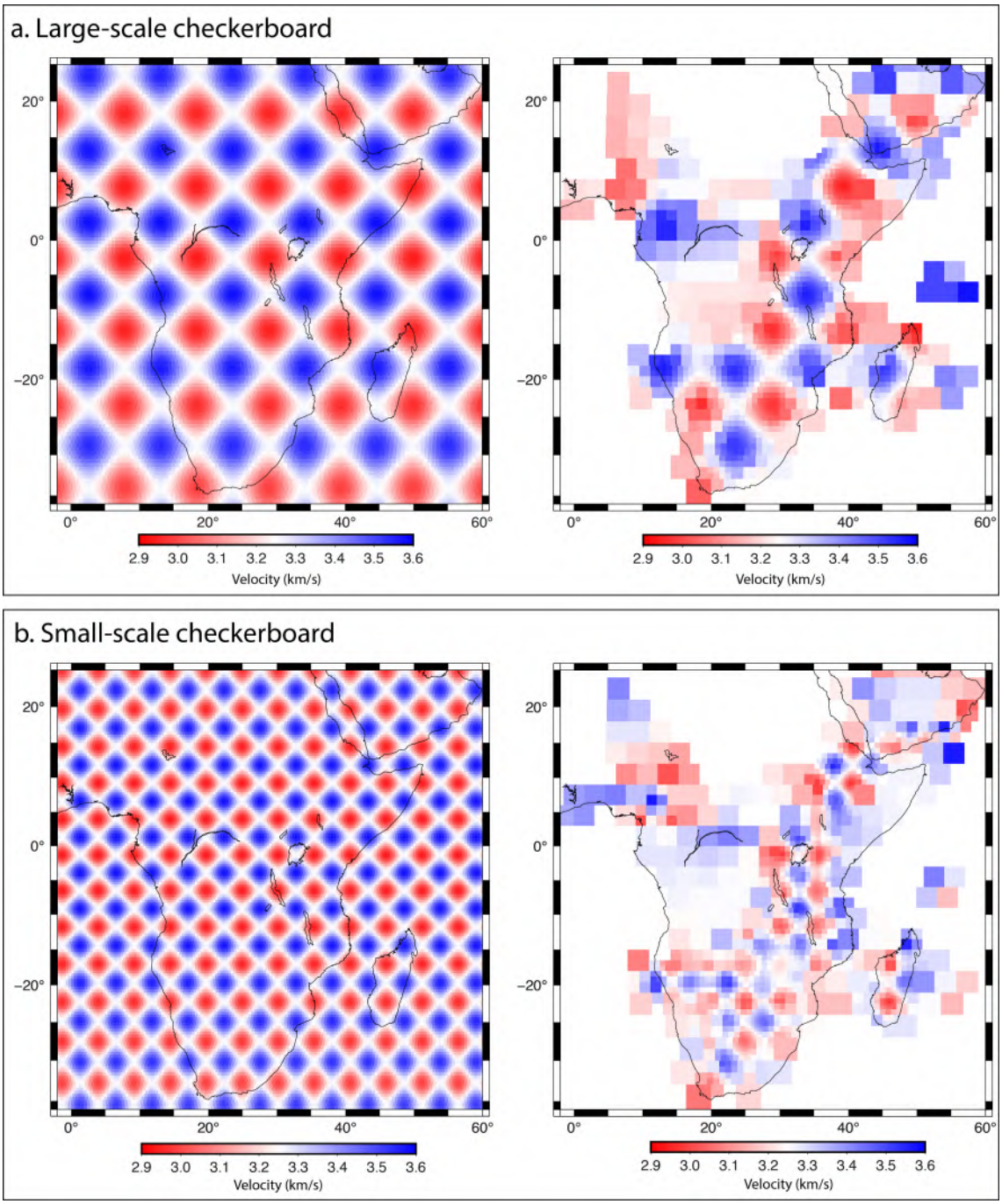

Figure 8. Checkerboard tests at 10 s. a. Large-scale checkerboard test. Left panel shows the input model (6 ° x 6° anomalies separated by a 1.5° gap), solution model is to the right. b. Small-scale checkerboard test. Left panel shows the input model (3 ° x 3° anomalies separated by a 0.75° gap), solution model is to the right.

increased resolution in this area relatively to other global studies (e.g. Ekström, 2011; Auer et al., 2014; Ruan et al., 2019). A comparison of resolution tests over Africa using (i) the global dataset and (ii) the global and regional dataset are found as Supporting Information. We additionally show another map at 10 s, computed from the regional dataset only, and centered on the EARS (fig. 11).

Rayleigh-wave phase-velocity maps show velocity anomalies at discrete periods. We can use the sensitivity kernels as shown in figure 12c to understand the depth range that can be resolved at each period. At 10s, the sensitivity kernel peak is above 20 km depth, meaning that the Rayleigh-waves mainly sample the crust. At 50 s, the peak is around 65 km depth, so the maps show velocity anomalies that reflect the structure of the crust and the uppermost mantle. For larger period we present in this study Rayleigh-waves mainly sample the upper mantle.

The adaptative grids calculated at each period are also shown in figure 9. The best illuminated areas are located in the Pacific Ocean, North America, Europe and Asia, because of a high seismicity and/or high concentration of permanent stations. As we added regional African networks to our global study, we increase the data coverage over eastern Africa. The adaptative grid thus displays smaller grid cells on this area.

Figure 10 shows ray-paths for the regional dataset at each period. The number of ray-paths for our regional dataset decreases from 25 to 100 seconds, as shown also in figure 3a. Noise data provide information mainly on the eastern part of Africa, Madagascar and the Mozambique Channel. EQ ray-paths quantity is the highest at 50 seconds, and provide informations on eastern Africa as well as in the Indian Ocean. Global ray-path density from Ekström (2011) increases from 25 s to 100 s (fig. 10).

Figure 11b is a 2D Rayleigh-wave phase velocity map at 10 s. At this period, we can resolve crustal structures. This map has been computed without the addition of global data, and thus displays the inversion of only regional data. Ray-paths at 10 s (fig. 11a) show that we have a very high density of rays above the EARS region, southern Africa, southern Arabia and Madagascar.

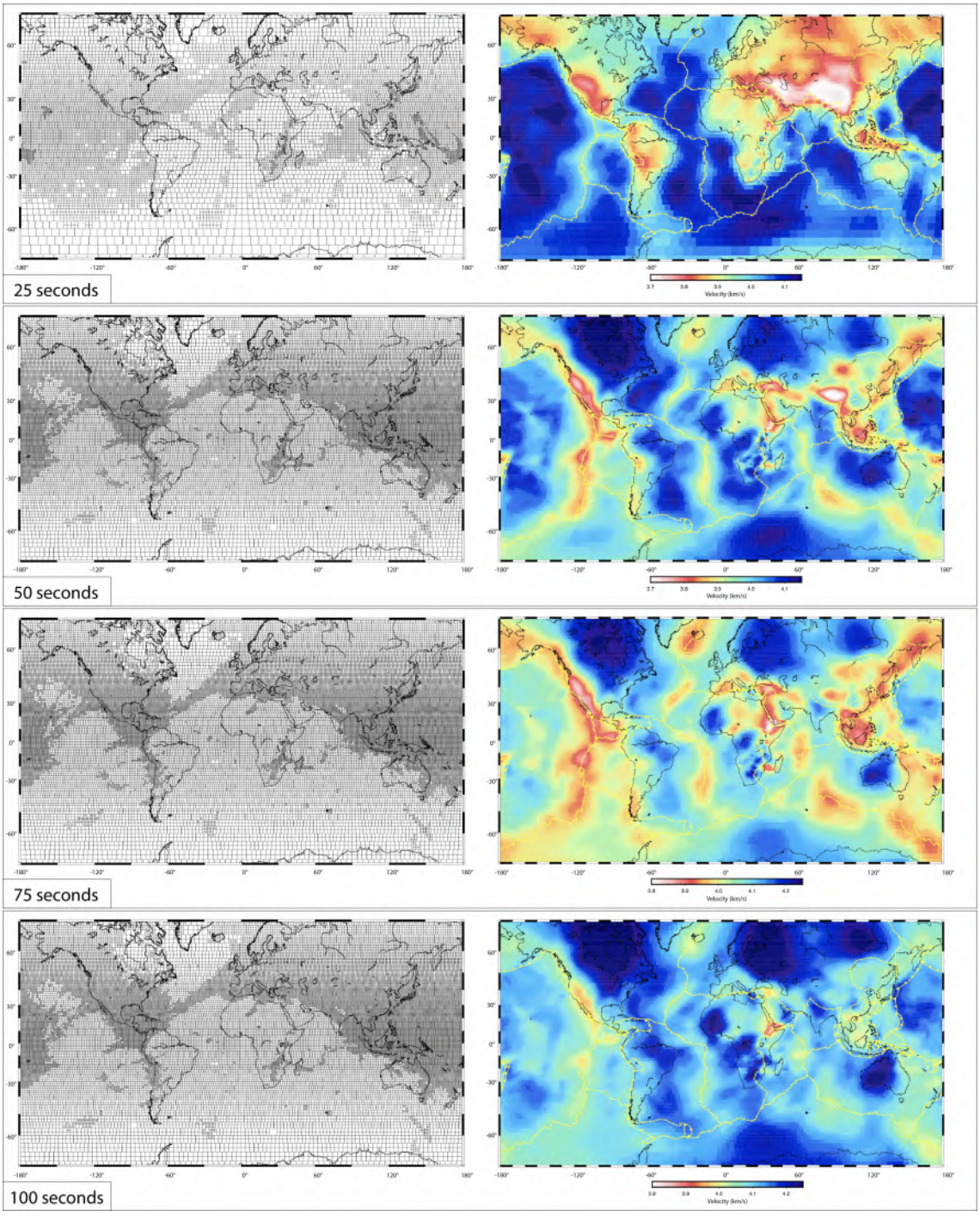

Figure 9. 2D Rayleigh wave phase velocity maps at 25, 50, 75 and 100 s. Plate boundaries from Bird (2003).

4.2.1 The East African Rift System

On previous global studies, the main visible feature of Africa was the Afar low-velocity anomaly, suggesting the presence of a mantle plume under the Afar triple junction (Ekström, 2011; Auer et al., 2014). Recent studies (Emry et al., 2019; Celli et al., 2020) show an improved resolution over the area: the Main Ethiopian Rift and a low-velocity anomaly beneath the Eastern Branch are identified. The regional study of Emry et al. (2019) even displays a low-velocity feature beneath the Kivu-Virunga Volcanic Province.

In our images (fig. 10 and 11b), we can better constrain these low-velocity anomalies. The lowest velocities are located in the Main Ethiopian Rift and western Afar depression, where the active volcano-tectonic segments and recent volcanoes are found (Ebinger & Casey, 2001). This low velocity feature is clearly visible as far as below the south-western Yemen and western Gulf of Aden volcanic margins, southern Red Sea, and the Afar region (Ahmed et al., 2013; Korostelev et al., 2014; Stab et al., 2016), where Tertiary volcanism can be found (fig. 1).

Further south, we do not observe a continuous low-velocity anomaly along the EARS, but several low-velocity zones. On the eastern branch, east of Lake Victoria, a first low-velocity zone is imaged from 10 to 75 s. This anomaly is located beneath the central graben of Kenya Rift, under a dozen of Quaternary volcanoes that are aligned along the Kenya rift valley. These volcanoes are known as the 'Quaternary Volcanic Province of central Kenya' (KQVP, fig. 12b) (B. Baker, 1987). KQVP probably represents the most recent activity in the most voluminous and extensive alkaline igneous province (Mechie et al., 1994). Tertiary and Quaternary volcanoes are shown in figures 1 and 12. The low-velocity anomaly is centered on recent volcanism in the area of the frequently erupting Greater Olkaria Volcanic Complex (Marshall et al., 2009) and Longonot volcano (fig. 12b), active this last millenium (last eruption in 1770 and 1863 respectively, according to Global Volcanism Program (2013)). The southern end of the low-velocity anomaly lies beneath three active volcanoes of the North Tanzanian divergence zone: Ol Doinyo Lengai, the famous unique low-temperature carbonatitic volcano in the world, Meru and Chyulu Hills volcanic field (fig. 12b). The low-velocity anomaly extends until Mount Kenya in the east.

The western branch is characterized by two low-velocity anomalies, located beneath the Kivu-Virunga and Rungwe Volcanic Province (respectively noted KVVP and RVP in fig. 12a).

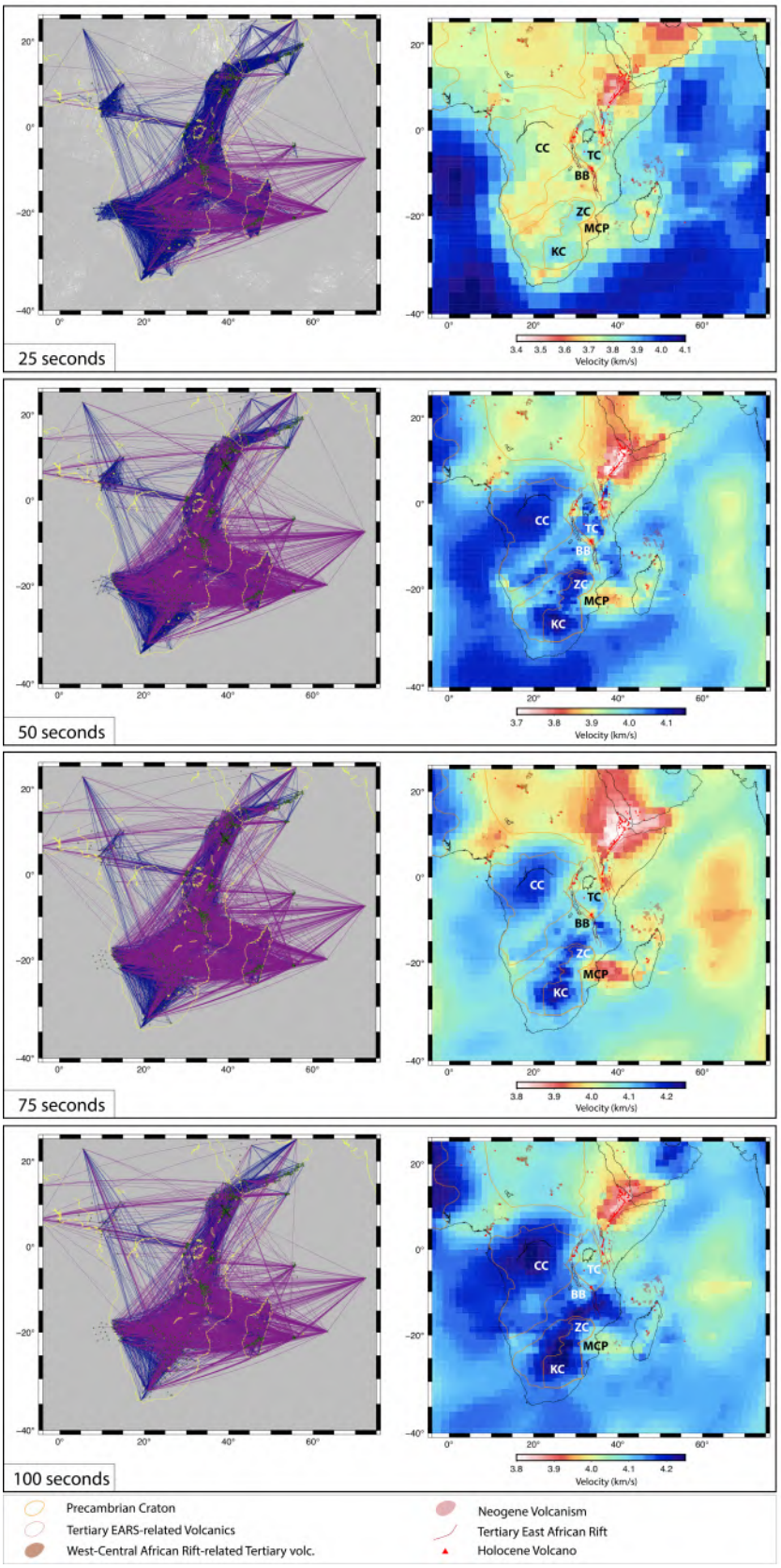

Figure 10. Left panels: ray-paths from regional dataset. Ray-paths from global dataset (Ekström, 2011) are shown in grey, ray-paths from ambient noise are shown in blue, ray-paths from teleseisms are shown in purple. Right panels: 2D Rayleigh wave phase velocity maps at 25, 50, 75 and 100 s. Abbreviations: BB Bangweulu Block, CC Congo Craton, KC Kaapval Craton,

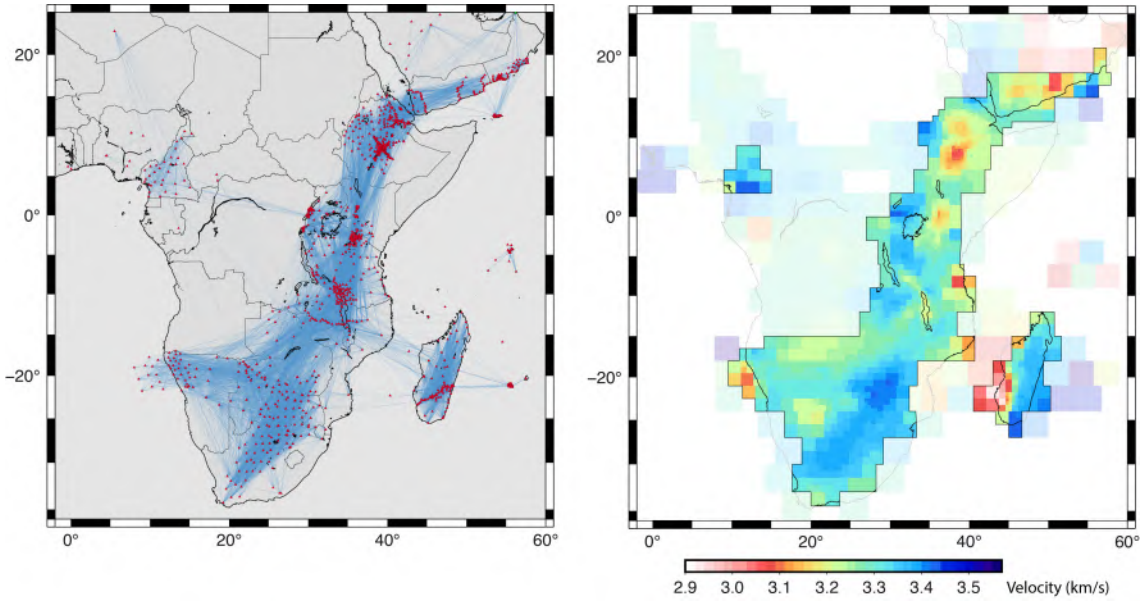

Figure 11. a. Ray-paths from regional ambient seismic noise dataset at 10 s. Sensors are shown in red. b. 2D Rayleigh wave phase velocity map at 10 s.

The Kivu-Virunga Volcanic Province (KVVP, fig. 12a) is located to the north of lake Kivu, in a transfer zone between two segments of the Western Branch of the EARS (Chorowicz, 2005). Moreover, the KVVP is located in the centre of the Kivu dome, a regional topographic uplift, which is thought to be related either to melting and lithospheric process in the underlying mantle (Chorowicz, 2005; Schmeling & Wallner, 2012) or to a local effect of mantle upwelling located beneath the nearby Tanzanian craton (Furman & Graham, 1999). Our maps display a relatively weak low-velocity anomaly from 25 to 75 s (∼3.9 km/s at 50 s) under this area (fig. 10 and 12a), although active volcanism is present since 10 Ma (Pasteels et al., 1989). Two of the most active volcanoes of Africa are even located in KVVP: Nyamuragira and Nyiragongo (fig. 12b) that hosts a semi-permanent lava lake (Samsonov & d'Oreye, 2012). The small amplitude of the retrieved anomaly could be due to relatively scarce data coverage in this region, which is centered on the edge of the temporary networks installed in the area (fig. 10 and 11).

The southernmost volcanic province in the Western Branch is the Rungwe Volcanic Province (RVP, fig. 12a), active from Miocene (Ebinger, 1989; O'Connor et al., 2019) and located at the northern tip of Malawi rift. This province is characterized by three large active volcanoes: Ngozi, Rungwe, and Kyejo (fig. 12b). In our maps, RVP is associated

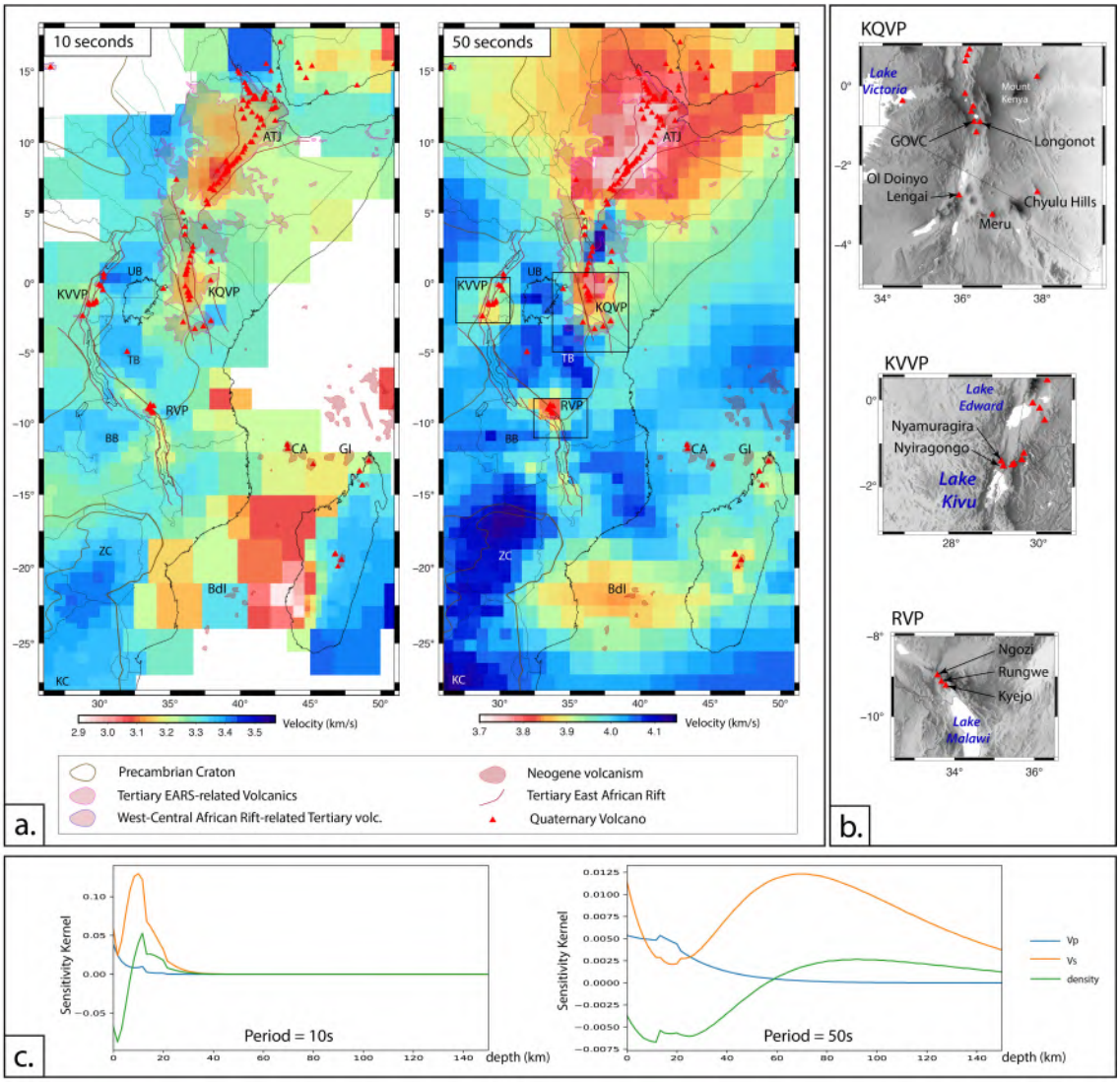

Figure 12. a. Rayleigh-wave phase-velocity map at 10 and 50 s. Abbreviations: ATJ Afar Triple Junction, BB Bangweulu Block, CA Comores Archipelago, BdI Bassas da India, KC Kaapval Craton, KQVP Kenya Quaternary Volcanic Province, KVVP Kivu-Virunga Volcanic Province, RVP Rungwe Volcanic Province, TB Tanzanian Block, UB Uganda Block, ZC Zimbabwe Craton. Structures are from Globig et al. (2016), volcanoes modified from Global Volcanism Program (2013). b. Zoom over the volcanic provinces. c. Sensitivity kernels at 10 and 50 s. At 10 s, best sensitivity is achieved between the surface and 20 km, which means that we can image crustal structures. At 50 s, best sensitivity is achieved between 40 and 100 km. We thus can image the structures of the crust and uppermost mantle. Kernels were calculated via Keurfon Luu's "disba" Python package.

with a pronounced low-velocity zone (∼3.83 km/s at 50 s, as seen in fig. 10) in the mantle from 25 to 75 s.

Finally, we observe the discontinuous nature of the EARS from north to south. Whereas the Afar Triple Junction appears as a large low-velocity mantle zone, the southern part of EARS is characterized by several patches of low-velocities in localized points. There, Quaternary volcanism occurred: Kivu-Virunga Volcanic Province, Kenya Quaternary Volcanic Province and Rungwe Volcanic Province are the three main volcanic area.

4.2.2 Mozambique Channel and Madagascar: the southern end of EARS?

Our Rayleigh-wave velocity maps highlight some interesting features beside the EARS and African cratons. Among them is a marked low-velocity anomaly in the Central Mozambique channel (BdI in fig. 12a). This low-velocity anomaly corresponds to a cluster of seamounts (some of the Eparses Islands): Europa platform, Bassas da India atoll, and Jaguar and Hall Banks. These islands and banks are tropical isolated shallow-water carbonate platforms (Courgeon et al., 2016). Morphology of crater and cones in the area suggests a volcanic origin, and dredgings have demonstrated the volcanic nature of these seamounts (Courgeon et al., 2016). However, no low-velocity anomaly have been imaged so far under the area. Our maps thus provide for the first time an evidence for the presence of hot mantellic material under the area, from 50 to 100 s. The Central Mozambique Channel is located in a diffuse zone of the southern EARS (Kusky et al., 2010), and the Bassas da India low-velocity is located in the direct continuity of the southern EARS onshore Africa. Moreover, as described in Torsvik and Cocks (2012, 2013), this part of the Mozambique Channel is located above the edges of the African large low shear-wave velocity province (LLSVP, in the deep mantle). The edges of the LLSVP are the plume generation zones, where the majority of plumes are generated (Torsvik & Cocks, 2012, 2013).

Northern part of Mozambique Channel hosts the Comoro Archipelago (CA in fig. 12a), composed of four volcanic islands (from west to east: Grande Comore, Mohély, Anjouan and Mayotte). Magmatism initiated ∼20 Ma ago in Mayotte (Emerick & Duncan, 1982; Michon, 2016) and is now giving birth to a new large submarine volcano located east of Mayotte (Lemoine et al., 2020; Feuillet et al., 2021). To the north-west, the Glorieuses Island (GI in fig. 12a) is the same kind of isolated carbonate platform with a volcanic origin (Courgeon

et al., 2016). Our maps image at 75 s a weak low-velocity anomaly under these clusters of islands and seamounts, centered on Glorieuses Islands (fig. 10).

Onshore Madagascar, the three small Quaternary volcanic regions are located in the northernmost tip of the island, its center and in the southwest. The northernmost volcanics seems to be aligned with the Comoro Archipelago and Glorieuses island volcanics. Our maps display a low velocity anomaly beneath this whole area, from 25 to 75 s. Another low-velocity anomaly lies beneath the center Madagascar volcanics from 25 to 75 s. And finally, the southwestern Madagascar volcanics are highlighted by the large Bassas da India low-velocity zone (BdI in fig. 12a) from 10 to 100 s (fig. 10 and 11b). Madagascar island has been rapidly uplifted since 30-40 Ma and seems to be maintained by mantle processes, in link with high asthenosphere temperatures and magmatism (Stephenson et al., 2021). These two low-velocity anomalies coincide with a zone of thinned lithosphere (Stephenson et al., 2021).

4.2.3 The African cratons

Global models show a clear correlation between fast velocities and the cratonic portions of the continents (e.g., Ekström, 2011). In our maps, fast velocities appear in the location of Archean cratonic lithosphere. These fast velocities are clearly distinct from 25 to 100 s. We thus observe that our study provides images of the distinct African cratons (Congo, Tanzanian, Zimbabwe and Kaapval cratons). It even seems possible to individualize some of the Archean blocks that were accreted during the life of the cratons.

The Tanzanian Craton (TC in fig. 12a) is composed of two smaller Archean fragments: the Uganda Block to the north and the Tanzanian Block to the south (Globig et al., 2016). The Tanzanian Craton is visible on our maps from 10 to 50 s for its northern part, and seems to be underlined by a weak low-velocity anomaly (visible at 75 and 100 s beneath Lake Victoria), also imaged in the study of Celli et al. (2020). In its southern part, fast velocities are observed at all periods, though they are less distinct from the velocities in the surrounding areas. In other studies (e.g. Weeraratne et al., 2003; Adams et al., 2018), a similar decrease in the amplitude of fast anomalies has been noted. Our image at 50 s suggests the presence of three different cratonic blocks within the Tanzanian Craton, located respectively under Lake Victoria (Uganda Block, UB in fig. 12a), in southwest and in southeast Tanzania Block (TB in fig. 12a). The northern block seems to be lying above

a weak low-velocity anomaly (at 75 and 100 s, fig. 10), whereas the two southern blocks display fast velocities until 100 s. This could mean that the northern block has a shallower lithospheric keel, which may reflect the thermal effect of nearby Kenya rift plume material (e.g. Nyblade et al., 2000; Weeraratne et al., 2003). The Archean Tanzanian Block seems to be composed of two smaller blocks. These blocks have deeper keels as they display faster velocities at 75 and 100 s. They are located further from plume or small-scale upwellings, and may therefore have undergone less cratonic carving.

To the west, the Bangweulu Block (BB in fig. 12a) is a cratonic feature proposed to be an Archean terrain (De Waele et al., 2006; O'Donnell et al., 2013). Here it appears as a fast-velocity zone from 10 to 50 s, but seems to do not have a cratonic root. This is consistent with previous studies (O'Donnell et al., 2013; Celli et al., 2020). The Congo Craton is characterized by a large fast-velocity anomaly in our maps from 50 to 100 s under the Congo Basin (fig. 10). At 25 s, resolution may be too poor to image its structure.

The southernmost craton of Africa is the Zimbabwe-Kaapval Craton. It displays the fastest velocities of all cratons on our maps (up to ∼4.2 km/s at 50 s and ∼4.3 km/s at 100 s). At 10, 25, 50 and 75 s, our map show clearly the two different blocks: Zimbabwe Craton to the north (ZC in fig. 10 and 12a) and Kaapval Craton to the south (KC in fig. 10 and 12).

5 Conclusions

In this study, we downloaded publicly-available seismograms from 54 seismic networks and processed them to obtain dispersion curves, using both ambient noise and earthquakes. We additionally take advantage of a global-scale, relatively long period database of surface-wave dispersion measurements (Ekström, 2011). The compilation of data from earthquake events and seismic noise, and of regional and global data provides us with a good data coverage, maximizing data density in the EARS. We translated the dispersion curves into phase velocity maps using a linearized inversion based on the ray theory. Owing to the adaptive parameterization criterion, we obtained enhanced resolution in comparison to previous studies. Our joint inversion of the numerous regional networks together with a global dataset gave us new maps that highlight the discontinuous nature of magmatic activity along the EARS. We found high velocities in correspondence of the African cratons (Tanzanian, Congo, Zimbabwe and Kaapval Cratons). Our detailed maps show several smaller

high-velocity anomalies within these cratons, which we interpret as Archean blocks within them. Besides the Afar triple junction and Main Ethiopian Rift, we image low velocities in correspondence of three active volcanic provinces: the Kivu-Kirunga, Kenya and Rungwe Volcanic Provinces. Other low-velocity anomalies are found beneath Comores Archipelago and Madagascar, which we interpret as higher temperature mantle and/or melt in active volcanic areas. Interestingly, we also found low velocities in correspondence of the Mozambique channel beneath Bassas da India Islands ans seamounts. This feature is expected upon consideration of the geology of the region, but was not shown in previous studies. A future 3D study based on a larger regional dataset will be lead to localize more precisely these low velocity features in depth and better understand the magmatic plumbing system in the Mozambique Channel.

Acknowledgments

Félicie Korostelev was supported by a grant from the PAMELA project (2020-2021) and from Sorbonne Université. The PAMELA project (PAssive Margin Exploration Laboratories) is a scientific project led by Ifremer and TOTAL in collaboration with Université de Bretagne Occidentale, Université Rennes 1, Sorbonne Université, CNRS and IFPEN. Fabrizio Magrini was Funded by the Deutsche Forschungsgemeinschaft (DFG - German Research Foundation) under the Individual Research Project: SI 1748/4-1. We acknowledge the Incorporated Research Institutions for Seismology - IRIS (http://www.iris.edu), the GEOFON Global Seismic Network (https://geofon.gfz-potsdam.de), RESIF (https://www.resif.fr), and IPGP (http://www.ipgp.fr) which provided the data used in this study. The maps were implemented with the Generic Mapping Tools (GMT, Wessel et al. 2013). The data for the following networks are provided by the Incorporated Research Institutions for Seismology (IRIS) Data Management Center (http://www.iris.edu):

1C (https://doi.org/10.7914/SN/1C_2011),

2H (https://doi.org/10.7914/SN/2H_2009),

4H (https://doi.org/10.7914/SN/4H_2011),

5H (https://doi.org/10.7914/SN/5H_2011),

8A (https://doi.org/10.7914/SN/8A_2015),

AF (https://doi.org/10.7914/SN/AF),

BX (Botswana Seismological Network),

DW (https://doi.org/10.7914/SN/DW),

G (https://doi.org/10.18715/GEOSCOPE.G),

GT (https://doi.org/10.7914/SN/GT),

II (https://doi.org/10.7914/SN/II),

IU (https://doi.org/10.7914/SN/IU),

MR (Mauritius Seismic Network),

NJ (https://doi.org/10.7914/SN/NJ),

NR (https://doi.org/10.7914/SN/NR),

XA (https://doi.org/10.7914/SN/XA_1997),

XB (https://doi.org/10.7914/SN/XB_2005),

XD (https://doi.org/10.7914/SN/XD_1994),

XI (https://doi.org/10.7914/SN/XI_1995;

https://doi.org/10.7914/SN/XI_2000),

XJ (https://doi.org/10.7914/SN/XJ_2013),

XK (https://doi.org/10.7914/SN/XK_2012),

XM (Ethiopia-Afar Geoscientific Lithospheric Experiment 6TD Passive Array),

XV (https://doi.org/10.7914/SN/XV_2011),

XW (https://doi.org/10.7914/SN/XW_2009),

XZ (https://doi.org/10.7914/SN/XZ_2003),

YH (https://doi.org/10.7914/SN/YH_2010),

YJ (Ethiopia-Afar Geoscientific Lithospheric Experiment),

YQ (https://doi.org/10.7914/SN/YQ_2013),

YR (https://doi.org/10.15778/RESIF.YR1999; Dhofar Seismic Experiment II),

YY (https://doi.org/10.7914/SN/YY_2013),

ZE (https://doi.org/10.7914/SN/ZE_2007),

ZF (Afar Consortium Network),

ZK (https://doi.org/10.7914/SN/ZK_2009),

ZP (https://doi.org/10.7914/SN/ZP_2007),

ZT (https://doi.org/10.7914/SN/ZT_2015),

and ZV (https://doi.org/10.7914/SN/ZV_2014).

The data for the following networks are hosted by GEOFON (https://geofon.gfz-potsdam.de/):

1B (Uganda project),

6A (https://doi.org/10.14470/1N134371),

GE (https://doi.org/10.14470/TR560404),

XC (https://doi.org/10.14470/KP6443475642),
and ZE (https://doi.org/10.14470/MR7567431421).
The data for the following networks are hosted by RESIF (https://seismology.resif.fr/):
7C (https://doi.org/10.15778/RESIF.7C2009),
PF (https://doi.org/10.18715/REUNION.PF),
YA (https://doi.org/10.7914/SN/YA_2012),
YV (https://doi.org/10.15778/RESIF.YV2011),
and ZS (https://doi.org/10.15778/RESIF.ZS2007).

References

Adams, A., Miller, J., & Accardo, N. (2018). Relationships between lithospheric structures and rifting in the East African Rift System: A Rayleigh wave tomography study. *Geochemistry, Geophysics, Geosystems*, *19*(10), 3793–3810.

Ahmed, A., Tiberi, C., Leroy, S., Stuart, G. W., Keir, D., Sholan, J., ... Basuyau, C. (2013). Crustal structure of the rifted volcanic margins and uplifted plateau of Western Yemen from receiver function analysis. *Geophysical Journal International*, *193*(3), 1673-1690.

Auer, L., Boschi, L., Becker, T., Nissen-Meyer, T., & Giardini, D. (2014). Savani: A variable resolution whole-mantle model of anisotropic shear velocity variations based on multiple data sets. *Journal of Geophysical Research: Solid Earth*, *119*(4), 3006–3034.

Baker, B. (1987). Outline of the petrology of the Kenya rift alkaline province. *Geological Society, London, Special Publications*, *30*(1), 293–311.

Baker, B. H., Mohr, P. A., & Williams, L. A. J. (1972). Geology of the eastern rift system of Africa. *Geological Society of America Special Papers*.

Bastow, I., Nyblade, A., Stuart, G., Rooney, T., & Benoit, M. (2008). Upper mantle seismic structure beneath the Ethiopian hot spot: Rifting at the edge of the African low-velocity anomaly. *Geochem. Geophys. Geosyst*, *9*(12), Q12022.

Bastow, I., Stuart, G., Kendall, J., Ebinger, C., et al. (2005). Upper-mantle seismic structure in a region of incipient continental breakup: Northern Ethiopian Rift. *Geophysical Journal International*, *162*(2), 479–493.

Bell, K., & Dodson, M. (1981). The geochronology of the Tanzanian Shield. *The Journal of Geology*, *89*(1), 109–128.

Benoit, M., Nyblade, A., & VanDecar, J. (2006). Upper mantle P-wave speed variations beneath Ethiopia and the origin of the Afar hotspot. *Geology*, *34*(5), 329–332.

Bensen, G., Ritzwoller, M., Barmin, M., Levshin, A., Lin, F., Moschetti, M., ... Yang, Y. (2007). Processing seismic ambient noise data to obtain reliable broad-band surface wave dispersion measurements. *Geophysical Journal International*, *169*(3), 1239–1260.

Bird, P. (2003). An updated digital model of plate boundaries. *Geochemistry, Geophysics, Geosystems*, *4*(3).

Bodin, T., & Sambridge, M. (2009). Seismic tomography with the reversible jump algorithm. *Geophysical Journal International*, *178*(3), 1411–1436.

Borrego, D., Nyblade, A. A., Accardo, N. J., Gaherty, J. B., Ebinger, C. J., Shillington, D. J., ... others (2018). Crustal structure surrounding the northern Malawi rift and beneath the Rungwe Volcanic Province, East Africa. *Geophysical Journal International*, *215*(2), 1410–1426.

Boschi, L., & Dziewonski, A. M. (1999). High-and low-resolution images of the Earth's mantle: Implications of different approaches to tomographic modeling. *Journal of Geophysical Research: Solid Earth (1978–2012)*, *104*(B11), 25567–25594.

Boschi, L., Weemstra, C., Verbeke, J., Ekström, G., Zunino, A., & Giardini, D. (2013). On measuring surface wave phase velocity from station–station cross-correlation of ambient signal. *Geophysical Journal International*, *192*(1), 346–358.

Celli, N. L., Lebedev, S., Schaeffer, A. J., & Gaina, C. (2020). African cratonic lithosphere carved by mantle plumes. *Nature communications*, *11*(1), 1–10.

Chang, S., Merino, M., Van der Lee, S., Stein, S., & Stein, C. (2011). Mantle flow beneath Arabia offset from the opening Red Sea. *Geophysical Research Letters*, *38*(4), L04301.

Chang, S.-J., Kendall, E., Davaille, A., & Ferreira, A. M. (2020). The evolution of mantle plumes in East Africa. *Journal of Geophysical Research: Solid Earth*, *125*(12), e2020JB019929.

Chesley, J. T., Rudnick, R. L., & Lee, C.-T. (1999). Re-Os systematics of mantle xenoliths from the East African Rift: Age, structure, and history of the Tanzanian craton. *Geochimica et Cosmochimica Acta*, *63*(7-8), 1203–1217.

Chorowicz, J. (2005). The east African rift system. *Journal of African Earth Sciences*, *43*(1-3), 379–410.

Clutier, A., Gautier, S., & Tiberi, C. (2021). Hybrid local and teleseismic P-wave tomog-

raphy in North Tanzania: role of inherited structures and magmatism on continental rifting. *Geophysical Journal International*, *224*(3), 1588–1606.

Courgeon, S., Jorry, S., Camoin, G., BouDagher-Fadel, M., Jouet, G., Révillon, S., ... others (2016). Growth and demise of Cenozoic isolated carbonate platforms: New insights from the Mozambique Channel seamounts (SW Indian Ocean). *Marine Geology*, *380*, 90–105.

Curtis, A., & Snieder, R. (1997). Reconditioning inverse problems using the genetic algorithm and revised parameterization. *Geophysics*, *62*(5), 1524–1532.

Daly, M., Chorowicz, J., & Fairhead, J. (1989). Rift basin evolution in Africa: the influence of reactivated steep basement shear zones. *Geological Society, London, Special Publications*, *44*(1), 309–334.

Davaille, A., & Romanowicz, B. (2020). Deflating the LLSVPs: Bundles of Mantle Thermochemical Plumes Rather Than Thick Stagnant "Piles". *Tectonics*, *39*(10), e2020TC006265.

De Hoop, M. V., & van Der Hilst, R. D. (2005). On sensitivity kernels for 'wave-equation'transmission tomography. *Geophysical Journal International*, *160*(2), 621–633.

De Waele, B., Johnson, S., & Pisarevsky, S. (2008). Palaeoproterozoic to Neoproterozoic growth and evolution of the eastern Congo Craton: its role in the Rodinia puzzle. *Precambrian Research*, *160*(1-2), 127–141.

De Waele, B., Liégeois, J.-P., Nemchin, A. A., & Tembo, F. (2006). Isotopic and geochemical evidence of Proterozoic episodic crustal reworking within the Irumide Belt of south-central Africa, the southern metacratonic boundary of an Archaean Bangweulu Craton. *Precambrian Research*, *148*(3-4), 225–256.

Dziewonski, A. M., & Anderson, D. L. (1981). Preliminary reference Earth model. *Physics of the earth and planetary interiors*, *25*(4), 297–356.

Ebinger, C. (1989). Tectonic development of the western branch of the East African rift system. *Geological Society of America Bulletin*.

Ebinger, C. (2005). Continental break-up: the East African perspective. *Astronomy & Geophysics*, *46*(2), 2–16.

Ebinger, C., & Casey, M. (2001). Continental breakup in magmatic provinces: An Ethiopian example. *Geology*, *29*(6), 527–530.

Ekström, G. (2011). A global model of Love and Rayleigh surface wave dispersion and

anisotropy, 25-250 s. *Geophysical Journal International*, *187*(3), 1668–1686.

Ekström, G., Abers, G. A., & Webb, S. C. (2009). Determination of surface-wave phase velocities across USArray from noise and Aki's spectral formulation. *Geophysical Research Letters*, *36*(18), L18301.

Emerick, C., & Duncan, R. (1982). Age progressive volcanism in the Comores Archipelago, western indian Ocean and implications for Somali plate tectonics. *Earth and Planetary Science Letters*, *60*(3), 415–428.

Emry, E. L., Shen, Y., Nyblade, A. A., Flinders, A., & Bao, X. (2019). Upper mantle Earth structure in Africa from full-wave ambient noise tomography. *Geochemistry, Geophysics, Geosystems*, *20*(1), 120–147.

Feuillet, N., Jorry, S., Crawford, W., Deplus, C., Thinon, I., Jacques, E., ... others (2021). Birth of a large volcanic edifice through lithosphere-scale dyking offshore Mayotte (Indian Ocean). *Nature Geoscience*.

Fontijn, K., Williamson, D., Mbede, E., & Ernst, G. G. (2012). The Rungwe volcanic province, Tanzania–a volcanological review. *Journal of African Earth Sciences*, *63*, 12–31.

Furman, T., & Graham, D. (1999). Erosion of lithospheric mantle beneath the East African Rift system: geochemical evidence from the Kivu volcanic province. *Developments in Geotectonics*, *24*, 237–262.

Global Volcanism Program. (2013). *Volcanoes of the World. Smithsonian Institution* (Vol. v. 4.9.1 (17 Sep 2020)). Global Volcanism Program. Retrieved 12 oct 2020, from `https://doi.org/10.5479/si.GVP.VOTW4-2013.`

Globig, J., Fernàndez, M., Torne, M., Vergés, J., Robert, A., & Faccenna, C. (2016). New insights into the crust and lithospheric mantle structure of Africa from elevation, geoid, and thermal analysis. *Journal of Geophysical Research: Solid Earth*, *121*(7), 5389–5424.

Hansen, S. E., & Nyblade, A. A. (2013). The deep seismic structure of the Ethiopia/Afar hotspot and the African superplume. *Geophysical Journal International*, *194*(1), 118-124.

Jacobs, J., Pisarevsky, S., Thomas, R. J., & Becker, T. (2008). The Kalahari Craton during the assembly and dispersal of Rodinia. *Precambrian Research*, *160*(1-2), 142–158.

Kästle, E. D., Soomro, R. A., Weemstra, C., Boschi, L., & Meier, T. M. (2016). Two-receiver measurements of phase velocity: cross-validation of ambient-noise and earthquake-

based observations. *Geophysical Journal International*, *207*, 1493-1512.

Korostelev, F., Basuyau, C., Leroy, S., Tiberi, C., Ahmed, A., Stuart, G. W., ... others (2014). Crustal and upper mantle structure beneath south-western margin of the arabian peninsula from teleseismic tomography. *Geochemistry, Geophysics, Geosystems*, *15*(7), 2850–2864.

Korostelev, F., Weemstra, C., Leroy, S., Boschi, L., Keir, D., Ren, Y., ... Ayele, A. (2015). Magmatism on rift flanks: insights from Ambient-Noise Phase-velocity in Afar region. *Geophys. Res. Lett.*

Kusky, T. M., Toraman, E., Raharimahefa, T., & Rasoazanamparany, C. (2010). Active tectonics of the Alaotra–Ankay Graben System, Madagascar: possible extension of Somalian–African diffusive plate boundary? *Gondwana Research*, *18*(2-3), 274–294.

Laó-Dávila, D. A., Al-Salmi, H. S., Abdelsalam, M. G., & Atekwana, E. A. (2015). Hierarchical segmentation of the Malawi Rift: The influence of inherited lithospheric heterogeneity and kinematics in the evolution of continental rifts. *Tectonics*, *34*(12), 2399–2417.

Lemoine, A., Briole, P., Bertil, D., Roullé, A., Foumelis, M., Thinon, I., ... Hoste Colomer, R. (2020). The 2018–2019 seismo-volcanic crisis east of Mayotte, Comoros islands: seismicity and ground deformation markers of an exceptional submarine eruption. *Geophysical Journal International*, *223*(1), 22–44.

Lu, Y., Stehly, L., Paul, A., & Group, A. W. (2018). High-resolution surface wave tomography of the European crust and uppermost mantle from ambient seismic noise. *Geophysical Journal International*, *214*(2), 1136–1150.

Luo, Y., Yang, Y., Xu, Y., Xu, H., Zhao, K., & Wang, K. (2015). On the limitations of interstation distances in ambient noise tomography. *Geophysical Journal International*, *201*(2), 652–661.

Magrini, F., Diaferia, G., Boschi, L., & Cammarano, F. (2020). Arrival-angle effects on two-receiver measurements of phase velocity. *Geophysical Journal International*, *220*(3), 1838–1844.

Manya, S. (2011). Nd-isotopic mapping of the Archaean–Proterozoic boundary in southwestern Tanzania: Implication for the size of the Archaean Tanzania Craton. *Gondwana Research*, *20*(2-3), 325–334.

Marshall, A., Macdonald, R., Rogers, N., Fitton, J., Tindle, A., Nejbert, K., & Hinton, R. (2009). Fractionation of peralkaline silicic magmas: The greater olkaria volcanic

complex, Kenya Rift Valley. *Journal of Petrology*, *50*(2), 323–359.

McConnell, R. (1972). Geological development of the rift system of eastern Africa. *Geological Society of America Bulletin*, *83*(9), 2549–2572.

Mechie, J., Keller, G. R., Prodehl, C., Gaciri, S., Braile, L., Mooney, W. D., ... Sandmeier, K.-J. (1994). Crustal structure beneath the Kenya Rift from axial profile data. *Tectonophysics*, *236*(1-4), 179–200.

Meier, T., Dietrich, K., Stöckhert, B., & Harjes, H.-P. (2004). One-dimensional models of shear wave velocity for the eastern Mediterranean obtained from the inversion of Rayleigh wave phase velocities and tectonic implications. *Geophysical Journal International*, *156*(1), 45–58.

Michon, L. (2016). *The volcanism of the Comoros archipelago integrated at a regional scale* (Vols. 333–344). Springer.

Mohr, P. (1982). Musings on continental rifts. *Continental and oceanic rifts*, *8*, 293–309.

Nguuri, T., Gore, J., James, D., Webb, S., Wright, C., Zengeni, T., ... Group, K. S. (2001). Crustal structure beneath southern Africa and its implications for the formation and evolution of the Kaapvaal and Zimbabwe cratons. *Geophysical Research Letters*, *28*(13), 2501–2504.

Nyblade, A., Owens, T., Gurrola, H., Ritsema, J., & Langston, C. (2000). Seismic evidence for a deep upper mantle thermal anomaly beneath east Africa. *Geology*, *28*(7), 599.

O'Connor, J. M., Jokat, W., Regelous, M., Kuiper, K. F., Miggins, D. P., & Koppers, A. A. (2019). Superplume mantle tracked isotopically the length of Africa from the Indian Ocean to the Red Sea. *Nature communications*, *10*(1), 1–13.

O'Donnell, J., Adams, A., Nyblade, A., Mulibo, G., & Tugume, F. (2013). The uppermost mantle shear wave velocity structure of eastern Africa from Rayleigh wave tomography: Constraints on rift evolution. *Geophysical Journal International*, *194*(2), 961–978.

Paige, C. C., & Saunders, M. A. (1982). LSQR: An algorithm for sparse linear equations and sparse least squares. *ACM Transactions on Mathematical Software (TOMS)*, *8*(1), 43–71.

Pasteels, P., Villeneuve, M., De Paepe, P., & Klerkx, J. (1989). Timing of the volcanism of the southern Kivu province: implications for the evolution of the western branch of the East African Rift system. *Earth and Planetary Science Letters*, *94*(3-4), 353–363.

Plasman, M., Hautot, S., Tarits, P., Gautier, S., Tiberi, C., Le Gall, B., ... Gama, R. (2019). Lithospheric structure of a transitional magmatic to amagmatic continental

rift system—insights from magnetotelluric and local tomography studies in the north Tanzanian divergence, East African rift. *Geosciences*, *9*(11), 462.

Ring, U. (2014). The East African Rift System. *Austrian Journal of Earth Sciences*, *107*(1).

Ring, U., Betzler, C., & Delvaux, D. (1992). Normal vs. strike-slip faulting during rift development in East Africa: the Malawi rift. *Geology*, *20*(11), 1015–1018.

Ritsema, J., Deuss, A., Van Heijst, H., & Woodhouse, J. (2011). S40RTS: a degree-40 shear-velocity model for the mantle from new Rayleigh wave dispersion, teleseismic traveltime and normal-mode splitting function measurements. *Geophysical Journal International*, *184*(3), 1223–1236.

Ritsema, J., Heijst, H., & Woodhouse, J. (1999). Complex shear wave velocity structure imaged beneath Africa and Iceland. *Science*, *286*(5446), 1925.

Ruan, Y., Lei, W., Modrak, R., Örsvuran, R., Bozdağ, E., & Tromp, J. (2019). Balancing unevenly distributed data in seismic tomography: a global adjoint tomography example. *Geophysical Journal International*, *219*(2), 1225–1236.

Samsonov, S., & d'Oreye, N. (2012). Multidimensional time-series analysis of ground deformation from multiple InSAR data sets applied to Virunga Volcanic Province. *Geophysical Journal International*, *191*(3), 1095–1108.

Schaefer, J., Boschi, L., & Kissling, E. (2011). Adaptively parametrized surface wave tomography: methodology and a new model of the European upper mantle. *Geophysical Journal International*.

Schmeling, H., & Wallner, H. (2012). Magmatic lithospheric heating and weakening during continental rifting: A simple scaling law, a 2-D thermomechanical rifting model and the East African Rift System. *Geochemistry, Geophysics, Geosystems*, *13*(8).

Soomro, R., Weidle, C., Cristiano, L., Lebedev, S., Meier, T., & Group, P. W. (2016). Phase velocities of Rayleigh and Love waves in central and northern Europe from automated, broad-band, interstation measurements. *Geophysical Journal International*, *204*(1), 517–534.

Stab, M., Bellahsen, N., Pik, R., Quidelleur, X., Ayalew, D., & Leroy, S. (2016). Mode of rifting in magma-rich settings: Tectono-magmatic evolution of Central Afar. *Tectonics*, *35*(1), 2–38.

Stephenson, S. N., White, N., Carter, A., Seward, D., Ball, P., & Klöcking, M. (2021). Cenozoic dynamic topography of Madagascar. *Geochemistry, Geophysics, Geosystems*, *22*(6), e2020GC009624.

Torsvik, T. H., & Cocks, L. R. M. (2012). From wegener until now: the development of our understanding of earth's phanerozoic evolution (andré dumont medallist lecture 2012). *Geologica belgica*.

Torsvik, T. H., & Cocks, L. R. M. (2013). Gondwana from top to base in space and time. *Gondwana Research*, *24*(3-4), 999–1030.

Tukey, J. W. (1977). Exploratory data analysis. *Addison-Wesly, PA*, *2*.

Weeraratne, D. S., Forsyth, D. W., Fischer, K. M., & Nyblade, A. A. (2003). Evidence for an upper mantle plume beneath the Tanzanian craton from Rayleigh wave tomography. *Journal of Geophysical Research: Solid Earth (1978–2012)*, *108*(B9).

White-Gaynor, A., Nyblade, A., Durrheim, R., Raveloson, R., van der Meijde, M., Fadel, I., ... others (2020). Lithospheric Boundaries and Upper Mantle Structure Beneath Southern Africa imaged by P and S wave Velocity Models. *Geochemistry, Geophysics, Geosystems*, *21*(10), e2020GC008925.

Yao, H., van Der Hilst, R. D., & De Hoop, M. V. (2006). Surface-wave array tomography in SE Tibet from ambient seismic noise and two-station analysis—I. Phase velocity maps. *Geophysical Journal International*, *116*(2), 732–744.

Zhou, L., Xie, J., Shen, W., Zheng, Y., Yang, Y., Shi, H., & Ritzwoller, M. H. (2012). The structure of the crust and uppermost mantle beneath South China from ambient noise and earthquake tomography. *Geophysical Journal International*, *189*(3), 1565–1583.